Isogeometric analysis of thin Reissner-Mindlin plates and shells: Locking phenomena and generalized local $\bar{B}$ method

Qingyuan Hu[a,b], Yang Xia[c], Sundararajan Natarajan[d], Andreas Zilian[b], Ping Hu[c], Stéphane P.A. Bordas[e,b,*]

[a] *Department of Engineering Mechanics, Dalian University of Technology, Dalian 116024, P.R. China*
[b] *Department of Computational Engineering Sciences, Faculty of Sciences, Technology and Communication, University of Luxembourg, Luxembourg*
[c] *School of Automotive Engineering, Dalian University of Technology, Dalian 116024, P.R. China*
[d] *Integrated Modelling and Simulation Lab, Department of Mechanical Engineering, Indian Institute of Technology, Madras, Chennai-600036, India*
[e] *Visiting Professor, Institute of Research and Development, Duy Tan University, K7/25 Quang Trung, Danang, Vietnam*

Abstract

We propose a generalized local $\bar{B}$ framework, addressing locking in degenerated Reissner-Mindlin plate and shell formulations in the context of isogeometric analysis. Parasitic strain components are projected onto the physical space locally, i.e. at the element level, using a least-squares approach. The formulation is general and allows the flexible utilization of basis functions of different order as the projection bases. The present formulation is much cheaper computationally than the global $\bar{B}$ method. Through numerical examples, we show the consistency of the scheme, although the method is not Hu-Washizu variationally consistent. The numerical examples show that the proposed formulation alleviates locking and yields good accuracy for various thicknesses, even for slenderness ratios of 1×10^5, and has the ability to capture deformations of thin shells using relatively coarse meshes. From the detailed numerical study, it can be opined that the proposed method is less sensitive to locking and mesh distortion.

Keywords: Isogeometric, Reissner-Mindlin shell theory, shear locking, B-bar method, least squares

*Corresponding author
Email addresses: qingyuanhucn@gmail.com (Qingyuan Hu), stephane.bordas@gmail.com (Stéphane P.A. Bordas)

1. Introduction

The conventional (Lagrange-based) finite element method (FEM) employs polynomial basis functions to represent the geometry and the unknown fields. The commonly employed approximation functions are Lagrangian polynomials. However, these Lagrange polynomials are usually built upon a mesh structure which needs to be generated, from the CAD or Image file provided for the domain of interest. This mesh generation leads to the loss of certain geometrical features: e.g. a circle becomes a polyhedral domain. Moreover, Lagrange polynomials lead to low order continuity at the interface between elements, which is disadvantageous in applications requiring high order partial differential equations.

The introduction of isogeometric analysis (IGA) [1] provides a general theoretical framework for the concept of "design-through-analysis" which has attracted considerable attention. The key idea of IGA is to provide a direct link between the computer aided design (CAD) and the simulation, by utilizing the same functions to approximate the unknown field variables as those used to describe the geometry of the domain under consideration, similar to the idea proposed in [2]. Moreover, it also provides a systematic construction of high-order basis functions [3]. Note that, more recently, a generalisation of the isogeometric concept was proposed, whereby the geometry continues to be described by NURBS functions, as in the CAD, but the unknown field variables are allowed to live in different (spline) spaces. This lead to the concept of sub and super-geometric analysis, also known as Geometry Independent Field approximaTion (GIFT), described within a boundary element framework in [4] and proposed in [5, 6] and later refined in [7]. Related ideas, aiming at the construction of tailored spline spaces for local refinement were proposed recently in [8].

In the literature, the IGA has been applied to study the response of plate and shell structures, involving two main theories, viz., the Kirchhoff-Love theory and the Reissner-Mindlin theory. Thanks to the $\mathcal{C}^1$-continuity of the NURBS basis functions adopted in IGA, Kiendl *et al.* [9] developed an isogeometric shell element based on Kirchhoff-Love shell theory. The isogeometric Kirchhoff-Love shell element for large deformations was presented in [10]. The isogeometric Reissner-Mindlin shell element was implemented in [11], including linear elastic and nonlinear elasto-plastic constitutive behavior. The blended shell formulation was proposed to glue the Kirchhoff-Love structures with

Reissner-Mindlin structures in [12]. In addition, the isogeometric Reissner-Mindlin shell formulation that is derived from the continuum theory was presented in [13], in which the exact director vectors were used to improve accuracy. The solid shell was developed in [14], in this formulation the NURBS basis functions were used to construct the mid-surface and a linear Lagrange basis function was used to interpolate the thickness field.

The Kirchhoff-Love type elements are rotation-free and are only valid for thin structures. Due to the absence of rotational degrees of freedom (DoFs), special techniques are required to deal with the rotational boundary conditions [9, 15] and multi-patch connection [16]. Theoretically, the Reissner-Mindlin theory is valid for both thick and thin structures, however it is observed from the literature [11, 17] that both the FEM and the IGA approaches suffer from locking for thin structures when the kinematics is represented by Reissner-Mindlin theory, especially for lower order elements and coarse meshes. This has attracted engineers and mathematicians to develop robust elements that alleviates this pathology. Adam et.al. proposed a family of concise and effective selective and reduced integration (SRI) [18] rules for beams [19], plates and shells [20], and non-linear shells using T-splines [21] within the IGA framework. Elguedj et. al. [22] presented $\bar{B}$ method and $\bar{F}$ method to handle nearly incompressible linear and non-linear problems. The $\bar{B}$ method has been successfully applied to alleviate shear locking in curved beams [23], two dimensional solid shells [24], three-dimensional solid shells [25] and in nonlinear solid shell formulation [26]. Reviewing the literature of the $\bar{B}$ method since its appearance [27], one valuable contribution is the introduction of local $\bar{B}$ concept [25, 28], thanks to which lots of computational effort has been saved without too much accuracy loss. In addition, the equivalence between the $\bar{B}$ method and the mixed formulation were proved [23, 25]. Echter and Bischoff [17, 29] employed the DSG method [30] within the IGA framework to alleviate shear locking syndrome effectively. Other approaches include twist Kirchhoff theory [31], virtual element method [32], collocation method [33, 34], simple first order shear deformation theory [35], and single variable method [36, 37]. The above approaches have been employed with Lagrangian elements and IGA framework with varying order of success.

This paper builds on [28] for beam and rod structures using Timoshenko theory, aiming to develop a locking-free formulation for plates and shells governed by Reissner-Mindlin theory within

IGA framework. In order to alleviate the locking phenomena, the locking strains are projected onto lower order physical space by the least square method. The novel idea behind the formulation is to use multiple sets of basis functions to project the locking strains locally i.e. element-wise, instead of projecting globally i.e. all over the patch. The local projecting algorithm is inspired by the local $\bar{B}$ method [25] and also by the work of local least square method [38, 39]. These kind of formulations allow one to perform least-square projections locally, thereby reducing the computational effort significantly.

The outline of this paper is as follows: Section 2 gives an overview of Reissner-Mindlin theory for plates and shells. In Section 3, we present the novel approach, the generalized local $\bar{B}$ method to alleviate the locking (both shear and membrane) problems encountered in thin structures whilst employing Reissner-Mindlin formulation. The robustness, accuracy and the convergence properties are demonstrated with some benchmark examples in Section 4, followed by concluding remarks in the last section.

2. Theoretical formulation for Reissner-Mindlin plates and shells

2.1. Reissner-Mindlin shell model

In IGA, the parametric space is typically Cartesian, while the physical domain of the undeformed shell can be of complex shape, not necessarily rectangular. For simplicity, we consider a rectangular shell of length L, width ℓ and constant thickness h. The linear elastic material, assumed to be homogeneous and isotropic, is described by Young's modulus, E and Poisson's ratio ν. Figure (1) represents the mid-surface of the shell in the parametric and physical spaces.

The main difference between the Reissner-Mindlin and the Kirchhoff-Love shell theory is in the assumptions on the deformation behavior of the section and in the resulting independent kinematic quantities attached to the mid-surface in order to describe the deformation. According to the Reissner-Mindlin theory, a first order kinematic description is used in the thickness direction to account for the transverse shear deformations. Assuming a Cartesian coordinate system, any arbitrary point P in the shell structure is described by:

$$\boldsymbol{x}_P = \boldsymbol{x} + z\boldsymbol{n} \tag{1}$$

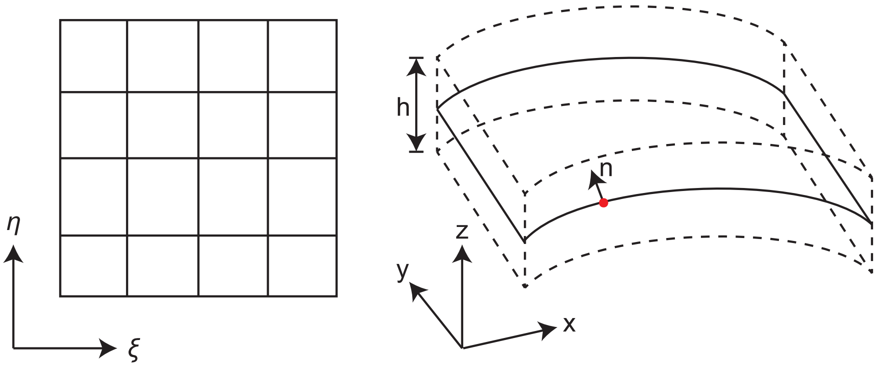

Figure 1: Mid-surface in the parameter space (left) and physical space (right) for a degenerated shell mid-surface. The real model is recovered by Eq.(1).

and its displacement is calculated assuming small deformation as

$$\boldsymbol{u}_P = \boldsymbol{u} + z\boldsymbol{\theta} \times \boldsymbol{n} \tag{2}$$

where $\boldsymbol{x}$ is the geometry of the mid-surface as shown in Fig.1, $z \in [-\frac{h}{2}, \frac{h}{2}]$ denotes the thickness. $\boldsymbol{u}$, $\boldsymbol{\theta}$ and $\boldsymbol{n}$ are the displacement vector, the rotation vector and the normal vector on the mid-surface point projected by point P. The linearized strain tensor valid for small deformations is adopted here

$$\boldsymbol{\varepsilon} = \frac{1}{2}(\boldsymbol{u}_{P,\boldsymbol{x}} + \boldsymbol{u}_{P,\boldsymbol{x}}^{\mathrm{T}}). \tag{3}$$

2.2. Isogeometric approach

In the context of shells, bi-variate NURBS basis functions are employed. Let $\Xi = \{\xi_1, \ldots, \xi_{n+p+1}\}$ and $H = \{\eta_1, \ldots, \eta_{m+q+1}\}$ be open knot vectors, and w_A be given weights, $A = \{1, \ldots, nm\}$. Then, the NURBS basis functions $R_A(\xi, \eta)$ are constructed, where p and q are the orders along the directions ξ and η respectively. For more details about IGA, interested readers are referred to [40] and references therein.

Following the degenerated type formulation, the geometry of the undeformed mid-surface is described by:

$$\boldsymbol{x} = \sum_{A=1}^{nm} R_A \boldsymbol{x}_A \tag{4}$$

and the mid-surface discrete displacement field is interpolated as:

$$\boldsymbol{U}^{\boldsymbol{h}} = \sum_{A=1}^{nm} R_A \boldsymbol{q}_A \tag{5}$$

where $\boldsymbol{x}_A$ defines the location of the control points, $\boldsymbol{U}^{\boldsymbol{h}} = (\boldsymbol{u}, \boldsymbol{\theta})^{\mathrm{T}}$, $\boldsymbol{q}_A = (\boldsymbol{u}_A, \boldsymbol{\theta}_A)^{\mathrm{T}}$ is the vector of control variables corresponding to each control point, specifically $\boldsymbol{u}_A = (u, v, w)^{\mathrm{T}}$ and $\boldsymbol{\theta}_A = (\theta_x, \theta_y, \theta_z)^{\mathrm{T}}$. The approximation space for displacement field is denoted as $Q_{p,q}$ in order to highlight the orders of the basis functions.

Once the mid-surface is described using Eq. (4) and Eq. (5), any arbitrary point P in the shell body can be traced by the following discrete forms:

$$\boldsymbol{x}_P = \sum_{A=1}^{nm} R_A (\boldsymbol{x}_A + z\boldsymbol{n}_A) \tag{6}$$

$$\boldsymbol{u}_P = \sum_{A=1}^{nm} R_A (\boldsymbol{u}_A + z\boldsymbol{\theta}_A \times \boldsymbol{n}_A) \tag{7}$$

where,

$$\boldsymbol{n} = \frac{\boldsymbol{x}_{,\xi} \times \boldsymbol{x}_{,\eta}}{||\boldsymbol{x}_{,\xi} \times \boldsymbol{x}_{,\eta}||_2} \tag{8}$$

is the normal vector. The normal vectors at the Greville abscissae $\boldsymbol{n}_A$ are adopted here because it can achieve a good balance between the accuracy and the efficiency [20]. It should be noted that the above equation includes the plate formulation, which can be considered as a special case. For plates, one always has $\boldsymbol{n}(x, y, z) = (0, 0, 1)^{\mathrm{T}}$, which means that there are only two rotational degrees of freedom, θ_x and θ_y.

Using Voigt notation, the relation between the strains and the stresses is expressed as

$$\boldsymbol{\sigma} = \boldsymbol{D}_g \boldsymbol{\varepsilon} \tag{9}$$

where $\boldsymbol{D}_g$ is the global constitutive matrix, and

$$\boldsymbol{D}_g = \boldsymbol{T}^{\mathrm{T}} \boldsymbol{D}_l \boldsymbol{T} \tag{10}$$

here $\boldsymbol{D}_l$ is the given local constitutive matrix. To make $\boldsymbol{D}_l$ suitable for the physical geometry, the transformation matrix $\boldsymbol{T}$ is employed, which is composed of $\boldsymbol{x}_{,\xi}$ and $\boldsymbol{x}_{,\eta}$.

Upon employing the Galerkin framework and using the following discrete spaces for the displacement field,

$$S = \left\{ \boldsymbol{U} \in \left[H^1(\Omega)\right]^d, \boldsymbol{U}|_{\Gamma_u} = \boldsymbol{U}^d \right\} \tag{11}$$

$$V = \left\{ \boldsymbol{V} \in \left[H^1(\Omega)\right]^d, \boldsymbol{V}|_{\Gamma_u} = 0 \right\}, \tag{12}$$

the variational function reads: find $\boldsymbol{U} \in S$ such that

$$b(\boldsymbol{U}, \boldsymbol{U}^*) = l(\boldsymbol{U}^*) \quad \forall \boldsymbol{U}^* \in V \tag{13}$$

in which the bilinear term is

$$b(\boldsymbol{U}, \boldsymbol{U}^*) = \int_{\Omega} \boldsymbol{\varepsilon}(\boldsymbol{U}^*)^{\mathrm{T}} \boldsymbol{D}_g \boldsymbol{\varepsilon}(\boldsymbol{U}) \mathrm{d}\Omega. \tag{14}$$

When the displacements and the rotations are approximated with polynomials from the same space, the discretized framework experiences locking (shear and membrane) when the thickness becomes very small. The numerical procedure fails to satisfy the Kirchhoff limit (thin shell) as the shear strain does not vanish with the thickness of the shell approaching zero. One explanation of shear locking is that different variables involved are not compatible [36], which is also known as field inconsistency. Recall Equation (2) and Equation (3), the field inconsistency only holds for plate formulation but not for shell formulation. However, it is observed that for the present shell formulation the element suffers from both membrane and shear locking. An explanation is that in curved elements shearless bending [41] and inextensible bending deformations cannot be represented exactly, because of the appearance of spurious membrane and shear terms that absorb the major part of the strain energy [23], and this results in an overestimation of the stiffness. In the next section, a locking-free Reissner-Mindlin plate/shell formulation is proposed within the framework of IGA.

3. Development of locking-free Reissner-Mindlin plates and shells

In this section, after introducing the classical $\bar{B}$ method, the numerical consistency is discussed. In order to further improve the efficiency and introduce flexibility into the formulation, a local and a generalized $\bar{B}$ form is proposed.

3.1. Classical B-bar method in IGA

The novel idea behind the $\bar{B}$ method is using a modified strain instead of the original one. It is believed that the modified strain should kept the numerical consistency and more importantly release the locking constrains thus have a better accuracy. In classical $\bar{B}$ method [22, 23], a common way is to use the projection of the original strain to formulate the bilinear term

$$\bar{b}(\boldsymbol{U}, \boldsymbol{U}^*) = \int_{\Omega} \bar{\boldsymbol{\varepsilon}}^{*\mathrm{T}} \boldsymbol{D} \bar{\boldsymbol{\varepsilon}} \mathrm{d}\Omega \tag{15}$$

The projected strain $\bar{\boldsymbol{\varepsilon}}$ and the original strain $\boldsymbol{\varepsilon}$ are equal in the sense of the least square projection. The projection space is chosen to be one order lower, i.e. $Q_{\bar{p},\bar{q}} = Q_{p-1,q-1}$ (see Figure (2)(a)). Built from one order lower knot vectors, with all the weights given as $W_{\bar{A}} = 1, \bar{A} = \{1, \ldots, \bar{n}\bar{m}\}$, one order lower B-spline basis functions $\bar{N}_{\bar{A}}$ are obtained. The L_2 projection process is performed on the physical domain as

$$\begin{aligned} &\int_{\Omega} \bar{N}_{\bar{B}} \left(\boldsymbol{\varepsilon}^h - \bar{\boldsymbol{\varepsilon}}^h \right) \mathrm{d}\Omega = 0 \\ &\bar{B} = 1, \ldots, \bar{n}\bar{m} \end{aligned} \tag{16}$$

in which the discretized form of the projected strain is

$$\bar{\boldsymbol{\varepsilon}}^h = \sum_{\bar{A}=1}^{\bar{n}\bar{m}} \bar{N}_{\bar{A}} \bar{\boldsymbol{\varepsilon}}^{\bar{A}h} \tag{17}$$

where $\bar{\varepsilon}^{\bar{A}^h}$ means the projection of ε^h onto $\bar{N}_{\bar{A}}$. Finally, we have

$$\bar{\varepsilon}^h = \sum_{\bar{A},\bar{B}=1}^{\bar{n}\bar{m}} \bar{N}_{\bar{A}} \boldsymbol{M}_{\bar{A}\bar{B}}^{-1} \int_\Omega \varepsilon^h \bar{N}_{\bar{B}} \mathrm{d}\Omega \tag{18}$$

where $\boldsymbol{M}_{\bar{A}\bar{B}}$ is is the inner product matrix

$$\boldsymbol{M}_{\bar{A}\bar{B}} = (\bar{N}_{\bar{A}}, \bar{N}_{\bar{B}})_\Omega = \int_\Omega \bar{N}_{\bar{A}} \bar{N}_{\bar{B}} \mathrm{d}\Omega \tag{19}$$

The Hu-Washizu principle is utilized to prove the variational consistency of the $\bar{B}$ method, while the verification of the average strain demonstrates its numerical consistency. More details of these contributions are given in [22–24, 42]. The Hu-Washizu principle is written as

$$\delta \Pi_{HW}(\boldsymbol{U}, \tilde{\varepsilon}, \tilde{\sigma}) = \int_\Omega \delta \tilde{\varepsilon}^{\mathrm{T}} \boldsymbol{D} \varepsilon \mathrm{d}\Omega + \delta \int_\Omega \tilde{\sigma}^{\mathrm{T}} (\varepsilon - \tilde{\varepsilon}) \mathrm{d}\Omega - \int_{\Gamma_f} \boldsymbol{t} \delta \boldsymbol{U} \mathrm{d}\Gamma_f \tag{20}$$

Here, the displacement field $\boldsymbol{U} \in S$, the assumed strain $\tilde{\varepsilon} \in \left[L^2(\Omega)\right]^d$ and the assumed stress $\tilde{\sigma} \in \left[L^2(\Omega)\right]^d$. The constraint condition of the variational consistency is expressed as

$$\int_\Omega \delta \tilde{\sigma}^{\mathrm{T}} (\varepsilon - \tilde{\varepsilon}) \mathrm{d}\Omega = 0 \tag{21}$$

and in the $\bar{B}$ case

$$\int_\Omega \delta \bar{\varepsilon}^{h\mathrm{T}} \boldsymbol{D} \left(\varepsilon^h - \bar{\varepsilon}^h\right) \mathrm{d}\Omega = 0 \tag{22}$$

As for the numerical consistency, the constraint condition is expressed as

$$\int_\Omega \bar{N}_{\bar{C}} \left(\varepsilon^h - \bar{\varepsilon}^h\right) \mathrm{d}\Omega = 0 \tag{23}$$

Since the terms of the constitutive matrix $\boldsymbol{D}_g$ are constant at every quadrature point, and recalling Equation (16), it can be shown that Equation (22) and Equation (23) are satisfied. If the whole part of the original strain is projected, these two consistency conditions are both satisfied. However, if only part of the original strain, for instance the average of the original strain, is projected, then only the numerical consistency condition is satisfied according to [24]. This conclusion also stands for the proposed method in this paper. In addition, [23, 25] proved that the $\bar{B}$ method is equivalent to the mixed method.

3.2. Local and generalized $\bar{B}$ method for Reissner-Mindlin plates and shells

It is noticed that one needs to calculate the inverse of matrix $\boldsymbol{M}$ in Equation (18), which could be computationally expensive if the projection is applied globally. Thus, from a practical point of view, it is highly recommended to project the strains locally [25, 28], i.e. element-wise

$$\bar{\boldsymbol{\varepsilon}}_e^h = \sum_{\bar{A},\bar{B}=1}^{(\bar{p}+1)(\bar{q}+1)} \bar{N}_{\bar{A}} \boldsymbol{M}_{\bar{A}\bar{B}}^{-1} \int_{\Omega_e} \boldsymbol{\varepsilon}_e^h \bar{N}_{\bar{B}} \mathrm{d}\Omega \tag{24}$$

with

$$\boldsymbol{M}_{\bar{A}\bar{B}} = (\bar{N}_{\bar{A}}, \bar{N}_{\bar{B}})_{\Omega_e} = \int_{\Omega_e} \bar{N}_{\bar{A}} \bar{N}_{\bar{B}} \mathrm{d}\Omega. \tag{25}$$

Moreover, instead of projecting the strains onto $Q_{p-1,q-1}$, different sets of projection spaces are adopted in this work. This is called the *generalized strategy*, which could bring more flexibility into the formulation. The idea behind this generalized projection is that, with the opinion of projecting the original strains into the lower order space could release the locking constrains, we treat the corner, boundary and inner elements separately by using the lowest possible order of each element thus release the locking constrains as much as possible. The projection spaces need to be chosen carefully to avoid ill-condition or rand deficiency, readers interested in the corresponding mathematical theory is recommended to see [43], which is in the context of volume locking (nearly-incompressible) problems. Here, the strategy in our previous work [28] is extended to bi-dimensional cases. One difference between [28] and the present work is that in [28] the strain projection is performed within the parametric domain, while in present work the projection is performed within the physical domain as shown in Equation (24), which makes the present formulation more suitable for geometries of varied shapes. Specifically, for space $Q_{2,2}$, we adopt $Q_{1,1}$ for corner elements, $Q_{0,1}$ and $Q_{1,0}$ for boundary elements, and $Q_{0,0}$ for inner elements, as shown in Figure (2)(b).

For degenerated plates and shells, although the geometries are represented in two dimensions,

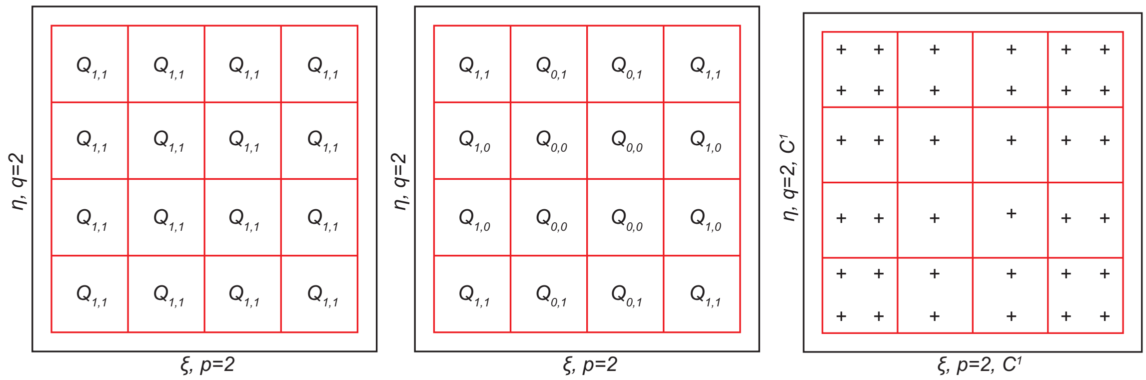

(a) Local $\bar{B}$ (b) Generalized local $\bar{B}$ (c) SRI [20]

Figure 2: Unlock strategies in bi-dimensional parameter space. Projecting spaces for locking strains are denoted as $Q_{p,q}$. For local $\bar{B}$ method (a), one order lower B-spline basis functions are employed for all elements. The presented generalized local $\bar{B}$ method (b) uses basis functions of different orders, inspired by the SRI method (c), while C^1 continuities of elements are not restricted as in (c).

there is the thickness z involved in the formulation. In this case, if the whole part of strain is projected, rank deficiency appears and the formulation yields inaccurate results as shown in [24] and also to our computational experience. Following the similar approach as outlined in [24, 25], in this work, only the average strain through the thickness is projected as

$$\overline{\boldsymbol{MID}(\boldsymbol{\varepsilon}_e^h)} = \sum_{\bar{A},\bar{B}=1}^{(\bar{p}+1)(\bar{q}+1)} \bar{N}_{\bar{A}} \boldsymbol{M}_{\bar{A}\bar{B}}^{-1} \int_{\Omega_e} \boldsymbol{MID}(\boldsymbol{\varepsilon}_e^h) \bar{N}_{\bar{B}} \mathrm{d}\Omega \tag{26}$$

where $\boldsymbol{MID}(\boldsymbol{\varepsilon}_e^h)$ is the average strain through the thickness within a single element

$$\boldsymbol{MID}(\boldsymbol{\varepsilon}_e^h) = \frac{1}{h} \int_{-\frac{h}{2}}^{\frac{h}{2}} \boldsymbol{\varepsilon}_e^h \mathrm{d}z. \tag{27}$$

The modified bi-linear form is defined as

$$\bar{b}(\boldsymbol{U}, \boldsymbol{U}^*) = \int_{\Omega} \left(\underbrace{\boldsymbol{\varepsilon}^{*\mathrm{T}} \boldsymbol{D} \boldsymbol{\varepsilon}}_{\text{original}} - \underbrace{\boldsymbol{MID}(\boldsymbol{\varepsilon}^*)^{\mathrm{T}} \boldsymbol{D} \boldsymbol{MID}(\boldsymbol{\varepsilon})}_{\text{average strain}} + \underbrace{\overline{\boldsymbol{MID}(\boldsymbol{\varepsilon})}^{\mathrm{T}} \boldsymbol{D} \overline{\boldsymbol{MID}(\boldsymbol{\varepsilon})}}_{\text{projected average strain}} \right) \mathrm{d}\Omega. \tag{28}$$

Within local $\bar{B}$, if the shape functions over the elements possess C^0 continuity (which is obviously fulfilled), the Hu-Washizu principle can be rewritten as [44]

$$\delta \mathit{\Pi}_{HW}(\boldsymbol{U}, \tilde{\boldsymbol{\varepsilon}}, \tilde{\boldsymbol{\sigma}}) = \sum_{m} \left(\int_{\mathit{\Omega}_m} \delta \tilde{\boldsymbol{\varepsilon}}^{\mathrm{T}} \boldsymbol{D} \boldsymbol{\varepsilon} \mathrm{d}\mathit{\Omega} + \delta \int_{\mathit{\Omega}_m} \tilde{\boldsymbol{\sigma}}^{\mathrm{T}} (\boldsymbol{\varepsilon} - \tilde{\boldsymbol{\varepsilon}}) \mathrm{d}\mathit{\Omega} - \int_{\mathit{\Gamma}_{fm}} \boldsymbol{t} \delta \boldsymbol{U} \mathrm{d}\mathit{\Gamma}_f \right) \tag{29}$$

in which m denotes the number of elements. In this context the assumed displacements should satisfy $\mathcal{C}^0$ continuous between elements, but discontinuous assumed strains are allowed, this explains why different sets of basis functions can be used. The constraint condition is expressed as

$$\int_{\mathit{\Omega}_m} \delta \tilde{\boldsymbol{\sigma}}^{\mathrm{T}} (\boldsymbol{\varepsilon} - \tilde{\boldsymbol{\varepsilon}}) \mathrm{d}\mathit{\Omega} = 0. \tag{30}$$

However, when the local $\bar{B}$ method is applied for degenerated plates, it is shown in the appendix of [24] that only the numerical consistency is satisfied, but the variational consistency is not satisfied.

3.3. Discussions

This generalized strategy is similar with the SRI strategy in [20]. The approach of using multiple sets of lower order basis functions was firstly presented for one-dimensional cases in [28]. In the case of only one quadrature point being used for an element, the functions are detected only at this quadrature point but nowhere else, which is analogous to its projection onto a $Q_{0,0}$ space. To achieve a better understanding of the proposed projection strategy, the basis functions are shown in Fig.3. There are four elements per side. In the local $\bar{B}$ method, only one single set of basis functions (i.e. $Q_{1,1}$) is used to form the projection space. While in the generalized local $\bar{B}$ method, four set of basis functions (i.e. $Q_{\bar{p},\bar{q}}$) are used. As shown in Fig.3 (b), this strategy means that the modified strains are assumed to be constant for the four internal elements and bi-linear for the four corner elements. In particular, for the side elements, the modified strains are assumed to be constant along the patch boundary, and linear facing inside. Moreover, it is noted that for cases of 1 element and 4 elements, there is no difference between the local $\bar{B}$ and generalized local $\bar{B}$.

The advantage of SRI method is that its implementation is simple and the computations involve less calculations because fewer quadrature points are employed. But one must consider the continuity between neighboring elements, which requires additional efforts. However, for the local $\bar{B}$ method, there is no problem in continuity because the projection procedure is applied element-

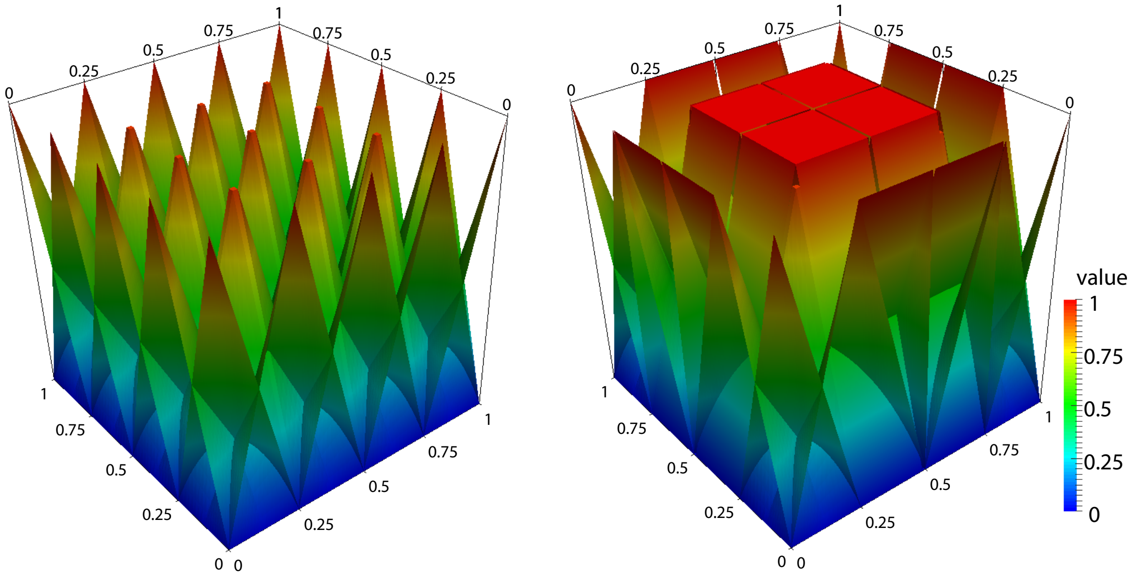

(a) Local $\bar{B}$ (b) Generalized local $\bar{B}$

Figure 3: Bi-dimensional basis functions for projecting locking strains of each element, let $Q_{p,q}$ denote the projecting space. There are 4×4 elements. (a) Basis functions of $Q_{1,1}$ in the local $\bar{B}$ method. (b) Basis functions in $Q_{\bar{p},\bar{q}}$ (see Fig.2) in the generalized local $\bar{B}$ method, the strains at the corners are assumed to be linear along both sides, the strains at the patch sides are assumed to be linear toward inside and constant along the boundary, the strains within the patch are assumed to be constant.

wise. This conclusion is also found in [28]. Thus, one could always use knot vectors of order $\bar{p}$ and continuity $C^{\bar{p}-1}$ (i.e. without inner repeated knots) as the projection knot vector. Apart from being accurate, since the lower order basis functions are used, for example linear functions for corner elements and constants for inner elements, better efficiency can be achieved with fewer quadrature points than usual.

Compared with the global $\bar{B}$ method, the local $\bar{B}$ method shows promising advantages in terms of computational efficiency. In the global $\bar{B}$ method, the calculation of the inverse of matrix $\boldsymbol{M}$ requires large amounts of memory. Thus, the adoption of local projection rather than global one saves lots of computational efforts. Similar conclusions had been carried out in the context of LLSQ fitting for boundary conditions [38] and further LLSQ algorithm [39]. In these contributions, assuming $\mathbf{A}$ is the global Boolean assembly operator, the matrix

$$\left(\mathbf{A}\mathbf{A}^{\mathrm{T}}\right)^{-1}\mathbf{A} \tag{31}$$

is used to calculate the uniformly weighted average of shared nodes. For instance, if a node (control point) is shared by n elements, then the values corresponding to this node is divided by n. Furthermore, in the local $\bar{B}$ method [25], same procedure named by strain smoothing is employed to ensure the continuity of the projected strains and thus to obtain results of better accuracy. The price to pay is that one need to calculate the average operator and the bandwidth is larger than classical IGA. In this research to obtain the strain field of higher order continuity, we use the original strain of discretized form ε^h instead of $\bar{\varepsilon}^h$, i.e. recover the displacement field firstly by Eq.(5) and then get the strain field as usual, in this way the continuity property of NURBS basis functions is utilized.

4. Numerical examples

In this section, we demonstrate the performance of the proposed generalized local $\bar{B}$ framework for Reissner-Mindlin plates/shells by solving a few standard benchmark problems. Unless otherwise mentioned consistent units are employed in this study. The numerical examples include: (a) Rectangular plate; (b) Scordelis-Lo roof; (c) Pinched cylinder and (d) Pinched hemisphere with a hole. In all the numerical examples, the following knot vectors are chosen as the initial ones:

$$\begin{aligned} \Xi &= \{0,0,0,1,1,1\} \\ H &= \{0,0,0,1,1,1\} \end{aligned} \tag{32}$$

In the following examples, $(p+1)\times(q+1)$ Gauss points are used for numerical integration, $p\times q$ Gauss points are used for the family of $\bar{B}$ methods for simplicity, the reduced quadrature scheme in [20] is adopted for comparison. The following conventions are employed whilst discussing the results:

- LB: Local $\bar{B}$ method without strain smoothing in Equation (31). The projection is applied element by element as shown in Eq.(24) and Figure (2)(a)

- GLB: Generalized local $\bar{B}$ method, which means that based on LB, the strategy of using multi-sets of basis functions as shown in Figure (2)(b) is adopted

- SRI: Selective reduced integration [20]

For the degenerated plates and shells, only the average strain through the thickness (Eq.(27)) is projected, thus the key word M is added and we have LBM and GLBM. The proposed formulation is implemented within the open source C++ IGA framework *Gismo* [1] [45].

4.1. Simply supported square plate

Consider a square plate simply supported on its edges with thickness h and the length of the side $L = 1$. Owing to symmetry, only one quarter of the plate, i.e, $a = L/2$ is modeled as shown in Figure (4). The plate is assumed to be made up of homogeneous isotropic material with Young's modulus $E = 200$ GPa and Poisson's ratio, $\nu = 0.3$. Two sets of loading are considered: (a) a point load P at the center of the plate and (b) uniform pressure. The control points and the corresponding weights are given in Table 1.

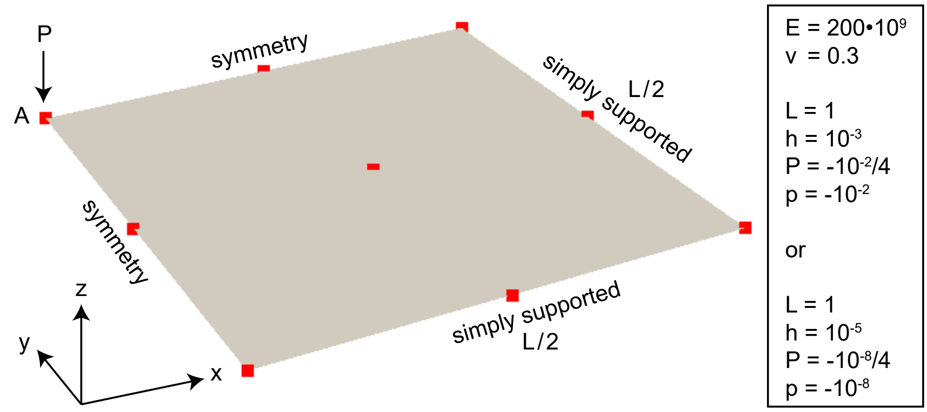

Figure 4: Mid-surface of the rectangular plate in Section 4.1: geometry and boundary conditions. Only one quarter of the plate is shown here. The red filled squares are the corresponding control points.

Table 1: Control points and weights for the rectangular plate in Figure (4).

	1	2	3	4	5	6	7	8	9
x	0.5	0.75	1	0.5	0.75	1	0.5	0.75	1
y	0	0	0	0.25	0.25	0.25	0.5	0.5	0.5
z	0	0	0	0	0	0	0	0	0
w	1	1	1	1	1	1	1	1	1

[1] https://ricamsvn.ricam.oeaw.ac.at/trac/gismo/wiki/WikiStart

The analytical out-of-plane displacements for a thin plate with simply supported edges are given by:

$$\text{Concentrated load}: \quad w(x,y) = \frac{4P}{\pi^4 D L^2} \sum_{m=1}^{\infty} \sum_{n=1}^{\infty} \frac{\sin\left(\frac{m\pi a}{L}\right)\sin\left(\frac{n\pi b}{L}\right)\sin\left(\frac{m\pi x}{L}\right)\sin\left(\frac{n\pi y}{L}\right)}{\left[\left(\frac{m}{L}\right)^2 + \left(\frac{n}{L}\right)^2\right]^2}$$

$$\text{Uniform pressure}: \quad w(x,y) = \frac{16p}{\pi^6 D} \sum_{m=1,3,5,\cdots}^{\infty} \sum_{n=1,3,5,\cdots}^{\infty} \frac{\sin\left(\frac{m\pi x}{L}\right)\sin\left(\frac{n\pi y}{L}\right)}{mn\left[\left(\frac{m}{L}\right)^2 + \left(\frac{n}{L}\right)^2\right]^2} \tag{33}$$

where $D = \frac{Eh^3}{12(1-\nu^2)}$. The transverse displacement is constant when the applied load is proportional to h^3, i.e. $P = P_o\,(h/h_o)^3$, where $P_o = 10$ and $h_o = 10^{-2}$ in this study. With this modification, the numerical solution does not depend on the thickness of the plate. For a plate bending problem with simply supported edges, the relationship between the Kirchhoff theory and the Mindlin theory can be obtained by the analogy of load equivalence as [46, 47]

$$w^M = w^K - \frac{D\nabla^2 w^K}{\kappa G h} \tag{34}$$

where w^K and w^M are the theoretical transverse deflection of the middle surface obtained by the Kirchhoff theory and Mindlin theory respectively, $\kappa = 5/6$ is the shear correction factor and $\nabla^2(\cdot) = \partial^2(\cdot)/\partial x^2 + \partial^2(\cdot)/\partial y^2$, w^K is given in Equation (33). Equation (34) is suitable for both thick and thin plates, because the second term tends to vanish when the thickness h becomes small. Theoretically, for a thin plate, one could obtain $w^M \approx w^K$. However, classical FEM and IGA elements using Mindlin theory suffers from shear locking syndrome. This is because the spurious strains appear such that the stiffness matrix is overestimated.

Figure (5) shows the normalized displacement as a function of mesh refinement for two different plate thickness, the reference value is w_A = -6.33410 $\times$ 10^{-6}. For thickness $h = 10^{-3}$, although the conventional IGA yields inaccurate results for coarse meshes, the results tend to improve upon refinement. However, it suffers from shear locking syndrome when $h = 10^{-5}$. In this case the results seem remain horizontal with respect to number of control points, indicating that the elements are fully locked. For LBM and GLBM slight rank deficiency occur for coarse meshes. GLBM get quite good results when $h = 10^{-5}$. From the numerical study it is inferred that the proposed formulation alleviates shear locking phenomenon and yields accurate results even for thin plates with coarse meshes.

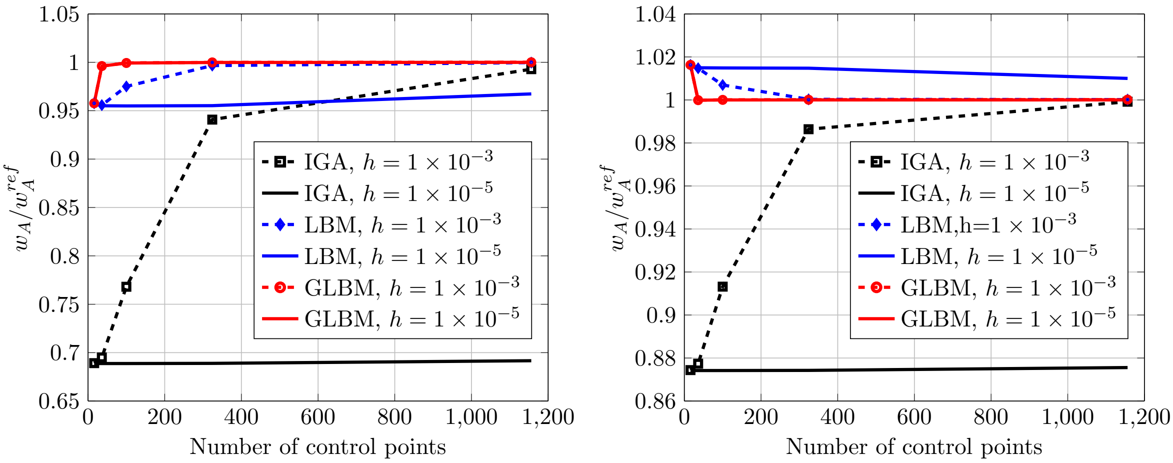

(a) Concentrated load (b) Uniform pressure

Figure 5: Normalized center displacement w_A with mesh refinement for the rectangular plate 4. LBM means local $\bar{B}$, GLBM means the generalized local $\bar{B}$, $h = 10^{-5}$ stands for thickness. IGA of order 2 suffer from locking. For LBM and GLBM rank deficiency occur for coarse meshes. GLBM gets good accuracy.

Figure (6) compares the convergence behavior by a severe locking case, in which the plate is subjected to concentrated load and its thickness is $h = 10^{-5}$. In this study, elements by IGA of order 2 are locked even by more than 1000 elements, the convergence rate is nearly zero. Elements by IGA of order 3 start with smaller error, but suffer from locking until the elements are refined to a certain number, specifically 361 control points in this case. It is inferred that classical IGA elements are locked until the elements are refined to a certain number, and higher order elements could reach this number earlier, this conclusion is already known in literatures. As discussed before, LBM behaves the same as GLBM for the first two refine steps, i.e. 9 control points and 16 control points respectively. GLBM achieves a good convergence rate at beginning, but in general the convergence rate is smaller as the meshes are refined, at the last two steps the errors become even larger, which is also observed for IGA of order 3 and order 4. Finally the errors seem to gather together.

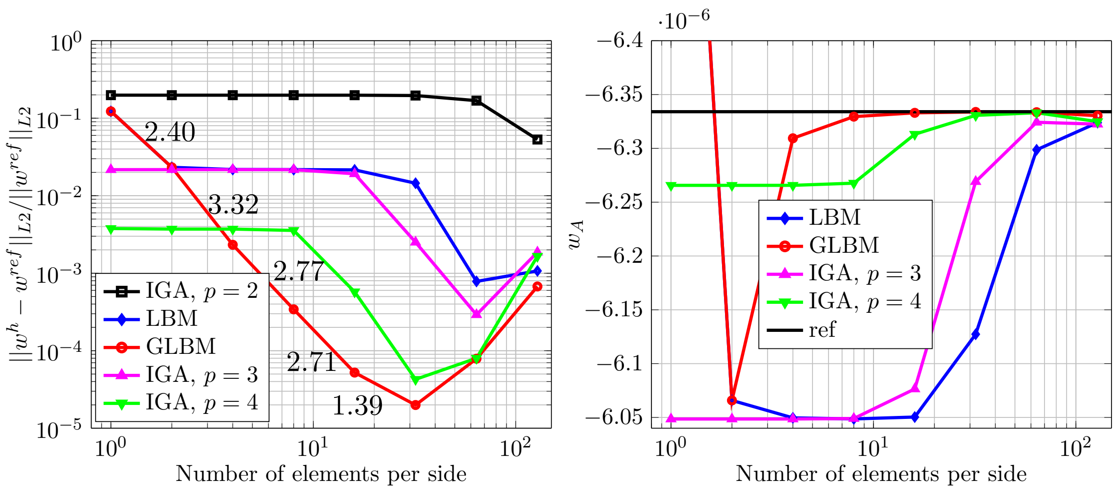

(a) Relative errors in L_2 norm of field w

(b) Solution w_A, partial enlarged.

Figure 6: The L_2 error of deflection w for the rectangular plate 4 subjected to concentrated load, thickness $h = 10^{-5}$. LBM means local $\bar{B}$, GLBM means the generalized local $\bar{B}$. IGA elements are locked until the elements are refined to a certain number. For GLBM in general the convergence rate is smaller as the meshes are refined, at the last two steps the errors become larger. Finally the errors seem to gather together.

To figure out why the errors become larger for very refined meshes in Figure (6), the errors of thicker plates are studied. However, for plate thickness larger than $h = 10^{-3}$, Equation (34) is expensive to use because the coefficient before $\nabla^2 w^K$ is much larger, which makes the solution difficult to converge. Due to the fact that the error of w_A can express the field error to some extent, for thicker plates only the errors of w_A are studied instead of the field error, and the reference solutions are obtained by commercial FEM software using 250000 four-node doubly curved shell elements with reduced integration and hourglass control. To be specific, for plate of thickness $h = 10^{-2}$ and concentrated force $P = 10$, the reference value is w_A = -6.39650 $\times$ 10^{-6}. Figure (7) show that for thicker plates the convergence rates seem more straight until the number of elements reach a certain value, and the results converges slower than thinner plates.

From the above, it is opined that for plates, only when the slenderness ratio reaches a large number, e.g. 10^3 or 10^5, the classical IGA elements suffer from locking. However, the studies above are done in an ideal condition that the plates are discreted by structured meshes. The influence of the mesh distortion on the performance of the proposed formulation is investigated by

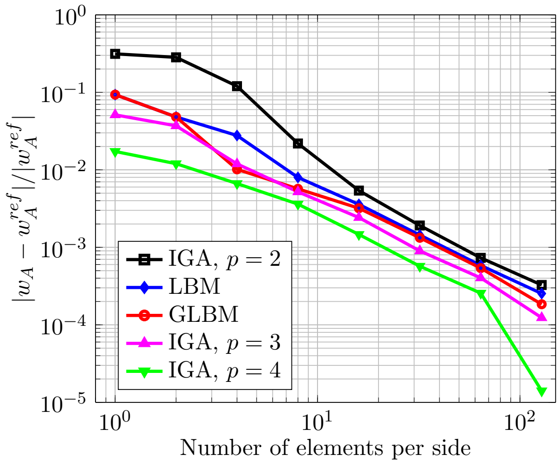

Figure 7: Relative errors of deflection w_A for the rectangular plate 4 subjected to concentrated load, thickness $h = 10^{-2}$. LBM means local $\bar{B}$, GLBM means the generalized local $\bar{B}$.

considering two different kinds of mesh distortions as shown in Figure (8). Thickness $h = 10^{-5}$ is considered here as the case when both locking and mesh distortion appear, and $h = 10^{-1}$ is chosen as the control case when only mesh distortion appears. The influence of mesh distortion on the normalized center displacement is depicted in Figure (9). When locking and mesh distortion occur at the same time, errors of IGA drop down quickly, while GLBM keeps good accuracy even for severe distortions. It can be inferred that the results with classical IGA deteriorates with mesh distortion, while the proposed formulation is less sensitive to the mesh distortion.

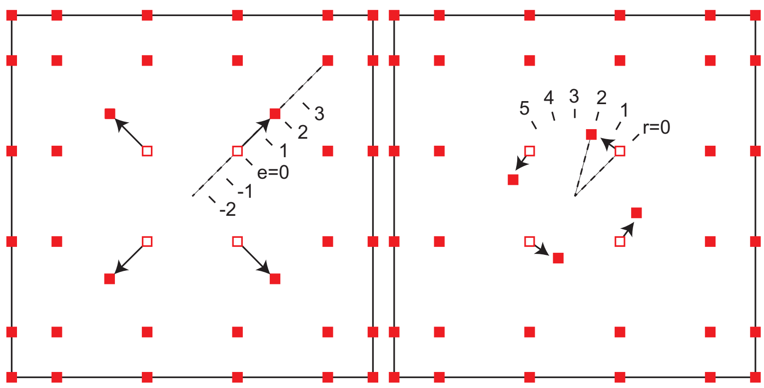

(a) Expansion

(b) Rotation

Figure 8: Illustration of control mesh distortions. In (a), four selected control points are moved along the diagonal. In (b), four selected control points are moved around the center of the patch. Indexes e and r are employed to indicate the stages of distortions.

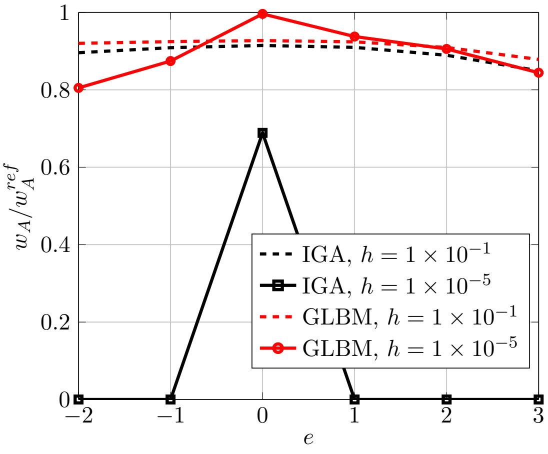

(a) Expansion e

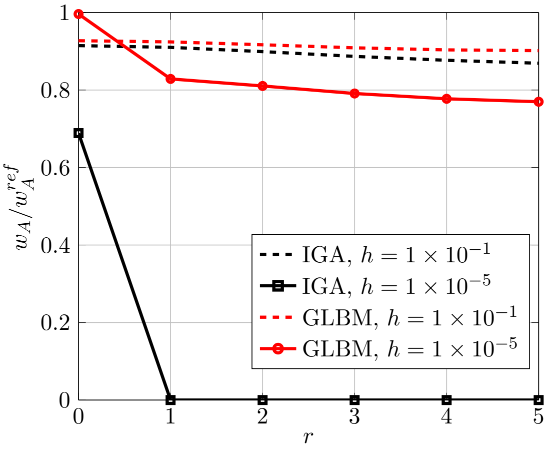

(b) Rotation r

Figure 9: Normalized results of w_A of the rectangular plate 4 with control mesh distortions 8. GLBM means the generalized local $\bar{B}$. h stands for thickness. When locking and mesh distortion occur at the same time, errors of IGA of order 2 drop down quickly, while GLBM keeps good accuracy even for severe distortions.

4.2. Scordelis-Lo roof

Next to demonstrate the performance of the proposed formulation when a structure experiences membrane locking, Scordelis-Lo roof problem is considered. It features a cylindrical panel with ends supported by rigid diaphragm. For the geometry considered here, $R/h = 100$ and $L/h = 200$, the structure experiences membrane locking as the transverse shear strain is negligible. The roof is dominated by membrane and bending deformations. Owing to symmetry only one quarter of the roof is modeled as shown in Figure (10). The roof is modeled with the control points (x, y, z) and the weights, w given in Table 2.

Table 2: Control points and weights for the Scordelis-Lo roof problem 10.

	1	2	3	4	5	6	7	8	9
x	0	1.091910703	1.928362829	0	1.091910703	1.928362829	0	1.091910703	1.928362829
y	0	0	0	1.5	1.5	1.5	3	3	3
z	3	3	2.298133329	3	3	2.298133329	3	3	2.298133329
w	1	0.9396926208	1	1	0.9396926208	1	1	0.9396926208	1

The roof is subjected to uniform pressure, $p_z = 6250$ N/m^2 and the vertical displacement of the mid-point of the side edge is monitored to study the convergence behavior. The analytical solution based on the deep shell theory w_B^{ref} = -0.0361 m [48] is taken as reference solution. The material properties are Young's modulus: $E = 30$ GPa and Poisson's ratio, $\nu = 0.0$. The convergence of the

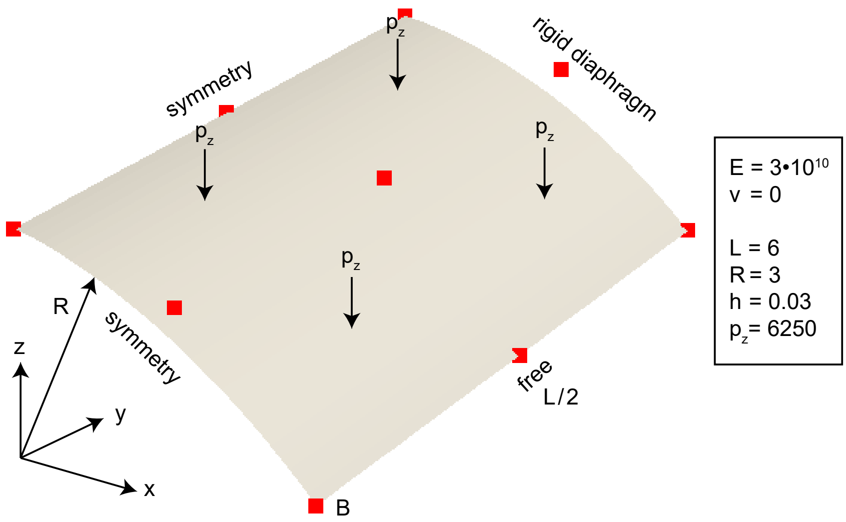

Figure 10: Scordelis-Lo roof problem in Section 4.2: geometry and boundary conditions. The red filled squares are the corresponding control points. The mid-surface of the cylindrical panel is modeled and the roof is subjected to a uniform pressure.

normalized vertical displacement with mesh refinement is shown in Figure (11). It is noticed that for coarse meshes the present method and local $\bar{B}$ method lead to rank deficient matrices, as in the strain smoothing method by a single subcell [49]. The results from the proposed formulation is compared with selective reduced integration technique [20]. It can be seen that except IGA of order 2, the convergence lines by others stall in the middle, while GLBM captures the stall first and then converge as before. In addition, the contour plot of the deflection w_B by IGA and GLBM are given in Figure (12) and Figure (13) as a function of mesh refinement. It is obvious that IGA is locked in the case of coarse mesh, while GLBM captures the deformation quite very well even for coarse meshes.

4.3. Pinched cylinder

From the above two examples, it is clear that the proposed formulation yields accurate results when the structure experience either shear locking or membrane locking. To demonstrate the robustness of the proposed formulation when the structure experiences both shear and membrane locking, we consider the pinched cylinder problem. The geometry of the cylinder is assumed to be same as the previous example. This example serves a test case to evaluate the performance when the structure is dominated by bending behaviour. Again, due to symmetry only one quarter of

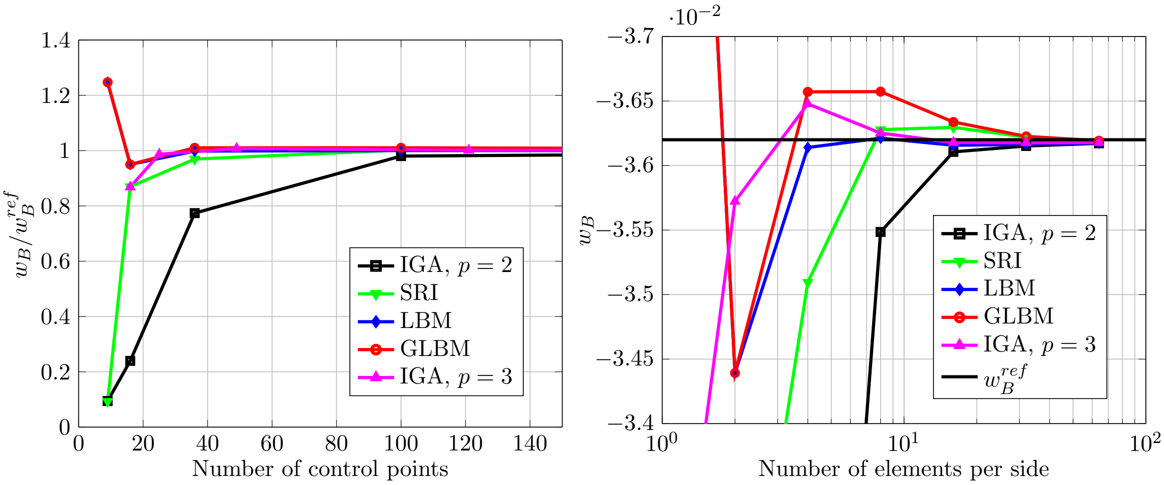

(a) Normalized results

(b) Solution w_B, partial enlarged.

Figure 11: Results of w_B of the Scordelis-Lo roof 10. LBM means local $\bar{B}$, GLBM means the generalized local $\bar{B}$. IGA suffers from locking. LBM and GLBM get slightly rank deficiency for coarse meshes, but finally converge. After a short stall, GLBM converges as before.

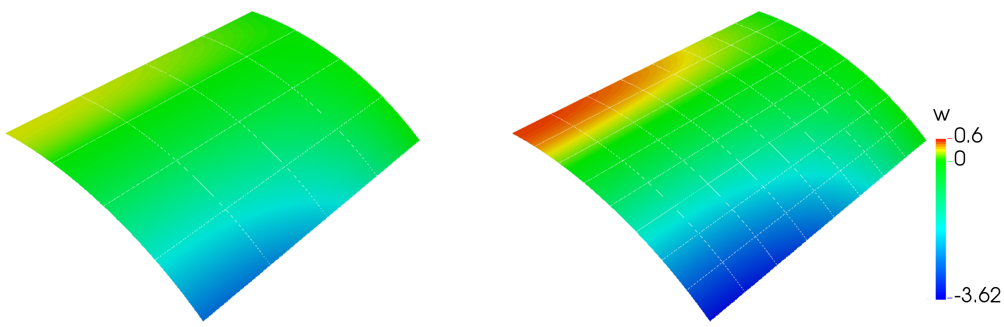

(a) 4×4 meshes

(b) 8×8 meshes

Figure 12: Deflection field $w \times 10^2$ of the Scordelis-Lo roof 10 by IGA. IGA is locked for coarse meshes.

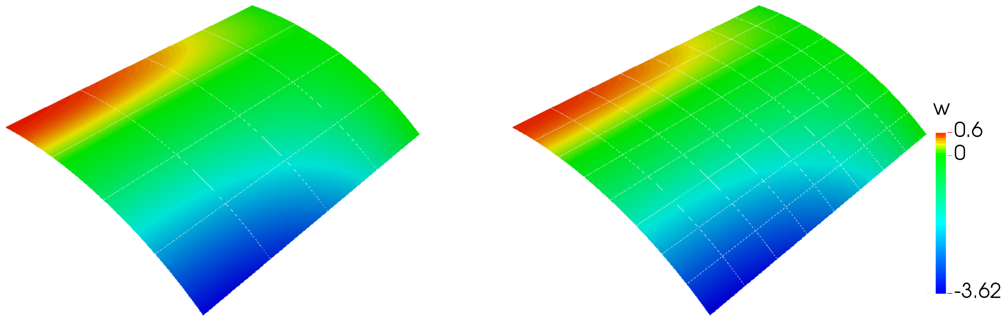

(a) 4×4 meshes

(b) 8×8 meshes

Figure 13: Deflection field $w \times 10^2$ of the Scordelis-Lo roof 10 by the generalized local $\bar{B}$. Deformation is captured very well for coarse meshes.

the cylinder is modeled as shown in Figure (14). The corresponding control points and weights are given in Table 3. The cylinder is made up of homogeneous isotropic material with Young's modulus, $E = 30$ GPa and Poisson's ratio, $\nu = 0.3$. The concentrated load acting on the cylinder is $P = 0.25$ N. The reference value of the vertical displacement is take as $w^{\text{ref}} =$ -1.8248e^{-7} m. The convergence of the vertical displacement with mesh refinement is shown in Figure (15) and it is evident that the proposed formulation yields more accurate results than the conventional IGA. All the used methods stall finally because they all mismatch the adopted reference value. The contour plot of w_C is shown in Figure (16) and Figure (17), the elements by GLBM seem more flexible than IGA to be deformed.

Table 3: Control points and weights for the pinched cylinder problem 14.

	1	2	3	4	5	6	7	8	9
x	0	3	3	0	3	3	0	3	3
y	0	0	0	1.5	1.5	1.5	3	3	3
z	3	3	0	3	3	0	3	3	0
w	1	0.7071067812	1	1	0.7071067812	1	1	0.7071067812	1

4.4. Pinched hemisphere with hole

As the last example, consider a pinched hemisphere with 18° hole subjected to equal and opposite concentrated forces applied at the four cardinal points. As before, owing to symmetry, only one quadrant of the hemisphere is modeled as shown in Figure (18). The location of the control points is also shown. The control points and weights employed to model the hemisphere

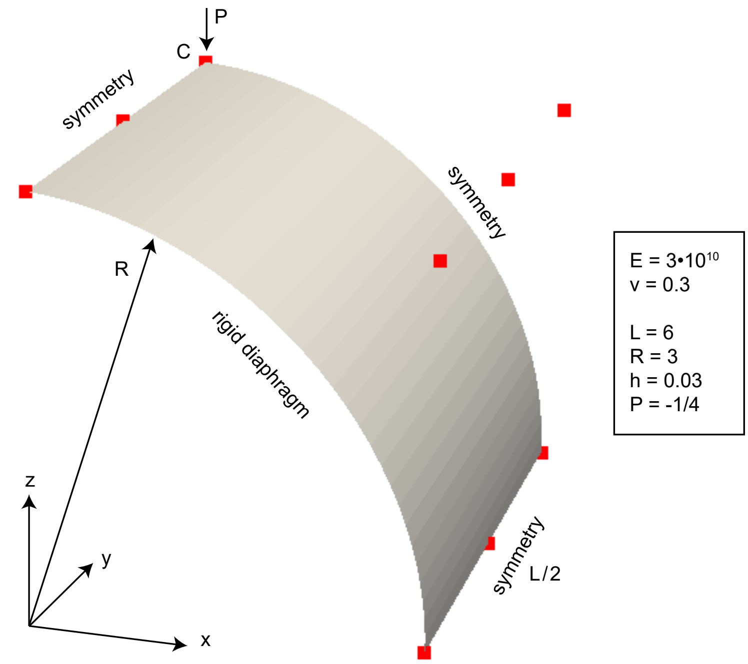

Figure 14: The mid-surface of a fourth of the pinched cylinder in Section 4.3. The red filled squares are the corresponding control points.

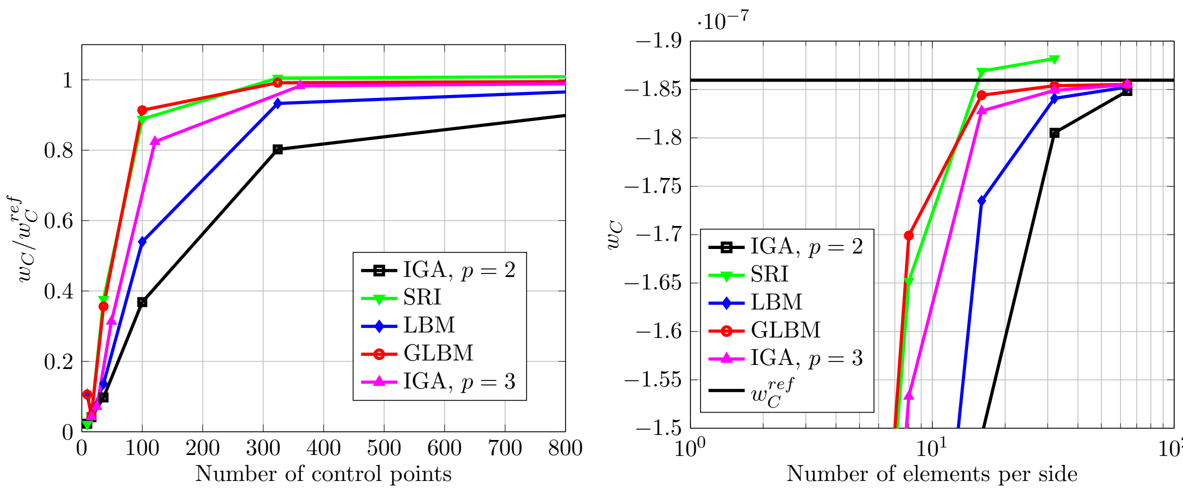

(a) Normalized results

(b) Solution w_C, partial enlarged.

Figure 15: Convergence of normalized vertical displacement with mesh refinement for the pinched cylinder 14. LBM means local $\bar{B}$, GLBM means the generalized local $\bar{B}$. GLBM achieves a good accuracy and convergence.

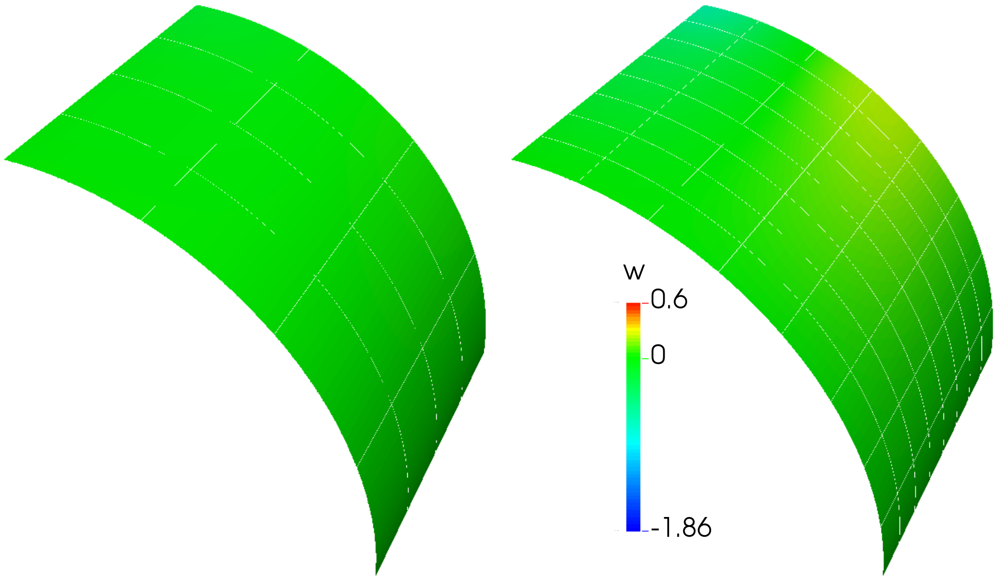

(a) 4×4 meshes

(b) 8×8 meshes

Figure 16: Field of $w \times 10^7$ of the pinched cylinder 14 by IGA. IGA is locked for coarse meshes and refined meshes.

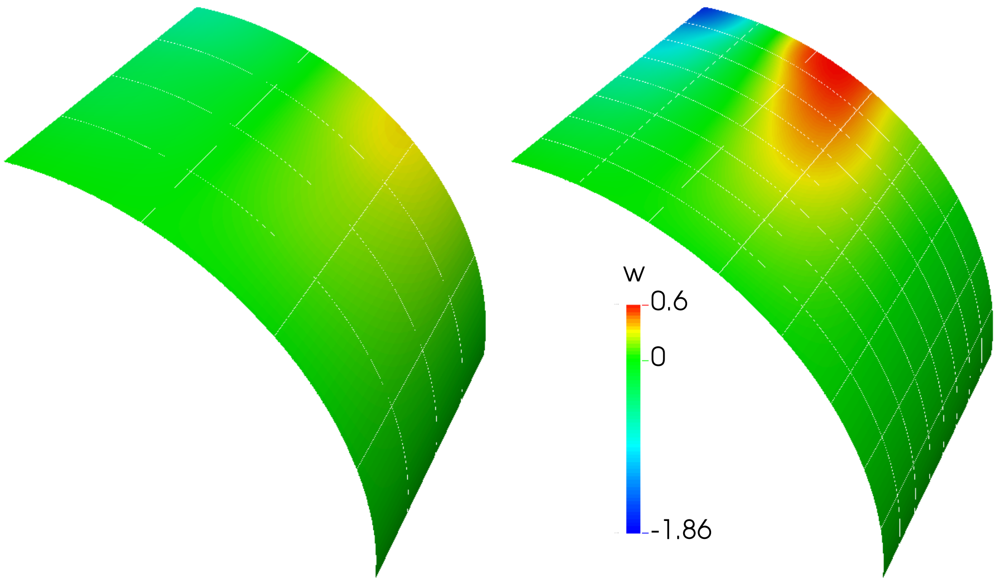

(a) 4×4 meshes

(b) 8×8 meshes

Figure 17: Field of $w \times 10^7$ of the pinched cylinder 14 by the generalized local $\bar{B}$ method. The elements seem more flexible than IGA to be deformed.

are given in Table 4. This example experiences severe membrane and shear locking, has right body rotations and the discretization experiences severe mesh distortion. The mesh distortion further enhances the locking pathology. To evaluate the convergence properties, the horizontal displacement $u_{\text{ref}} = 0.0940$ m is taken as the reference solution. The hemisphere is modeled with Young's modulus, $E = 68.25$ MPa, Poisson's ratio $\nu = 0.3$ and concentrated force, $P = 1$ N. The results form the proposed formulation are plotted in Figure (19), in which numerical instability of $\bar{B}$ methods (LBM and GLBM) is observed for the initial single element case. As the elements are refined, GLBM behaves similarly to SRI, but the results obtained by GLBM is slightly accurate. The reason that prevents the error to go below is the mismatch between the convergence value and the adopted reference value. Moreover, the field of displacement u_x is plotted in Figure (20) and Figure (21), it seems that GLBM has more abilities to capture the deformations.

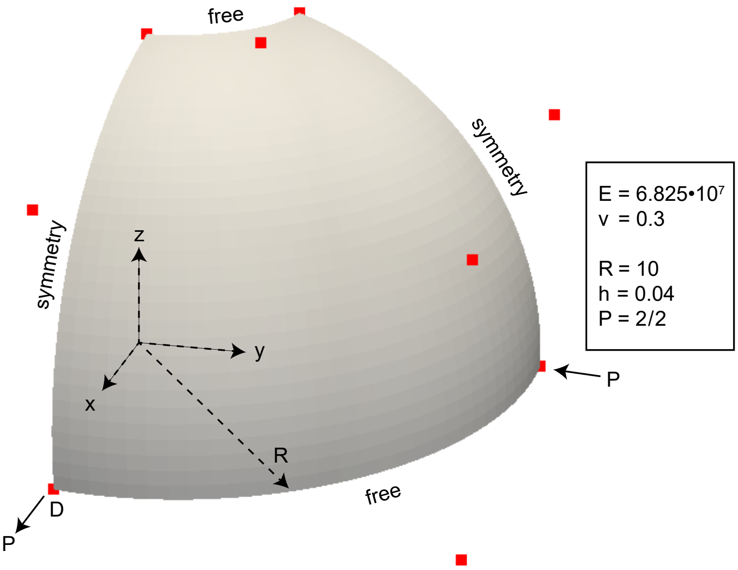

Figure 18: The mid-surface of a fourth of the pinched hemisphere in Section 4.4. The red filled squares are the corresponding control points.

Table 4: Control points and the corresponding weights for the pinched hemisphere problem 18.

	1	2	3	4	5	6	7	8	9
x	10	10	0	10	10	0	3.090169944	3.090169944	0
y	0	10	10	0	10	10	0	3.090169944	3.090169944
z	0	0	0	7.265425281	7.265425281	7.265425281	9.510565163	9.510565163	9.510565163
w	1	0.7071067810	1	0.8090169942	0.5720614025	0.8090169942	1	0.7071067810	1

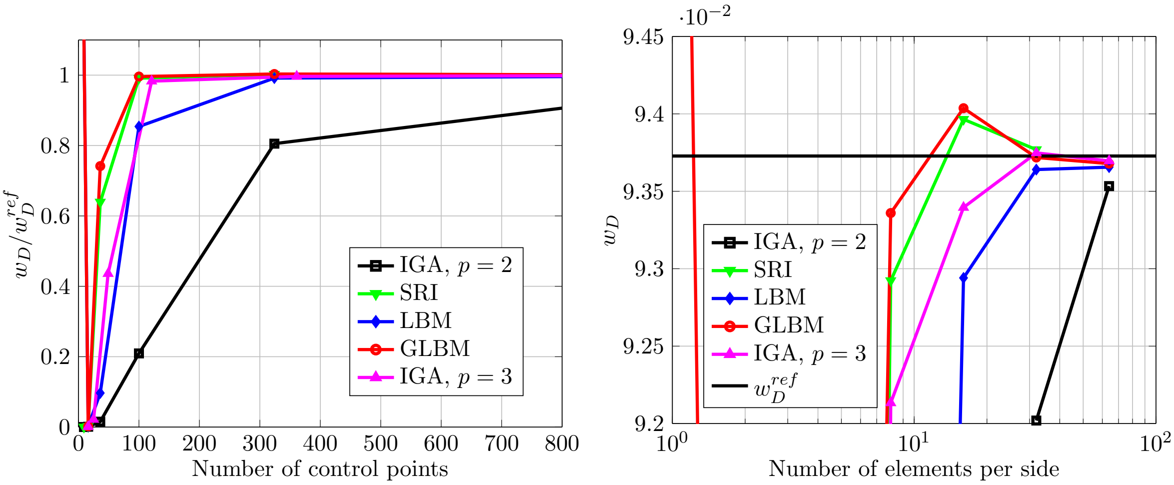

(a) Normalized results

(b) Solution u_D, partial enlarged.

Figure 19: Results of u_D of the pinched hemisphere 18. LBM means local $\bar{B}$, GLBM means the generalized local $\bar{B}$. Rank deficiency occur for coarse meshes by LBM and GLBM but they finally converge. GLBM gets good convergence performance.

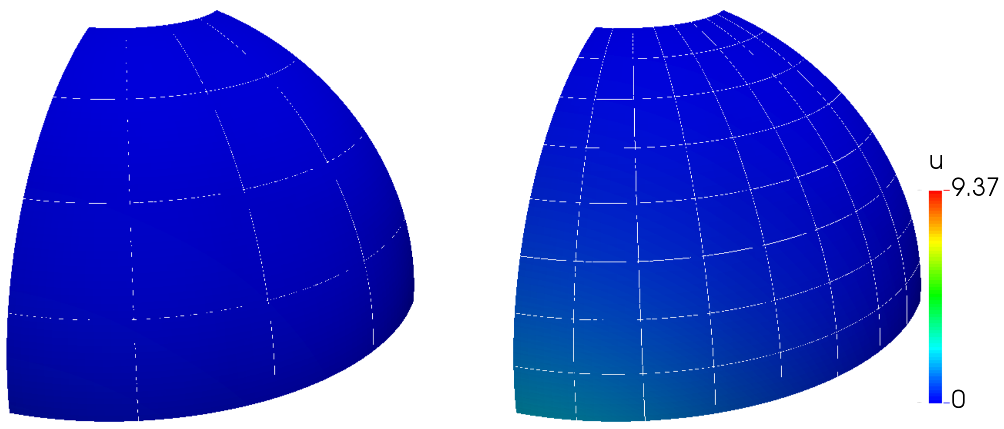

(a) 4×4 meshes

(b) 8×8 meshes

Figure 20: Field of $u_x \times 10^2$ of the pinched hemisphere 18 by IGA. Severe locking is noticed.

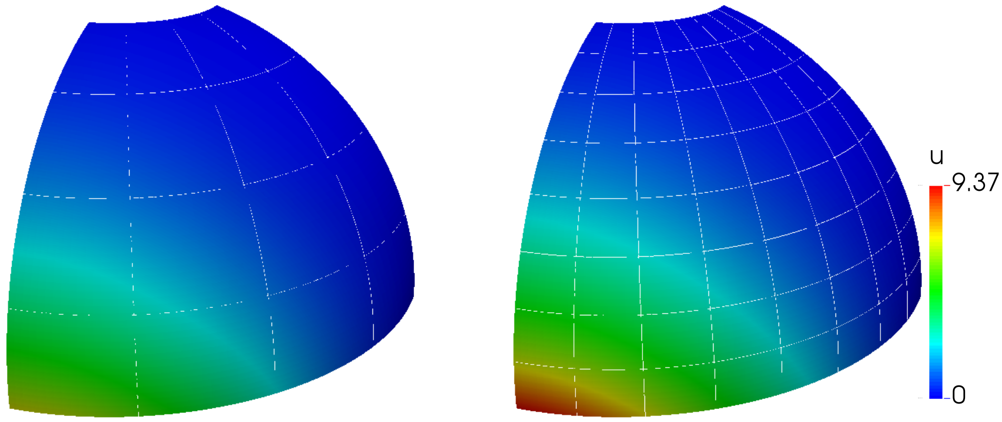

(a) 4×4 meshes

(b) 8×8 meshes

Figure 21: Field of $u_x \times 10^2$ of the pinched hemisphere 18 by the generalized local $\bar{B}$. Elements deform more easily.

5. Conclusion remarks

The generalized local $\bar{B}$ method is adopted to unlock the degenerated Reissner-Mindlin plate and shell elements within the framework of isogeometric analysis. The plate/shell mid-surface and the unknown field is described with non-uniform rational B-splines. The proposed method uses multiple sets of lower order B-spline basis functions as projection bases, by which the locking strains are modified in the sense of L_2 projection, in this way field-consistent strains are obtained.

The salient features of the proposed local $\bar{B}$ method are: (a) has less computational effort than global $\bar{B}$ and includes local $\bar{B}$; (b) yields better accuracy than classical IGA especially in cases of coarse meshes and mesh distortions; (c) suppresses both shear and membrane locking commonly encountered when lower order elements are employed and suitable for both thick and thin models; (d) for some cases of coarse meshes can lead to rank deficient matrices, as in the strain smoothing approach with a single subcell [49].

Future work includes extending the approach to large deformations, large deflections and large rotations as well as investigating the behaviour of the stabilization technique for enriched approximations such as those encountered in partition of unity methods [49–51].

Acknowledgments

Q. Hu is funded by China Scholarship Council and National Natural Science Foundation of China (No. 11272075). Y. Xia is funded by National Natural Science Foundation of China (No.61572021, 11272075). Stéphane Bordas thanks partial funding for his time provided by the European Research Council Starting Independent Research Grant (ERC Stg grant agreement No. 279578) "RealTCut Towards real time multiscale simulation of cutting in non-linear materials with applications to surgical simulation and computer guided surgery". We also thank the funding from the Luxembourg National Research Fund (INTER/MOBILITY/14/8813215/CBM/Bordas and INTER/FWO/15/10318764). Q. Hu is thankful for Prof. Gengdong Cheng for the valuable suggestions of this research subject.

References

[1] T. J. Hughes, J. A. Cottrell, Y. Bazilevs, Isogeometric analysis: Cad, finite elements, nurbs, exact geometry and mesh refinement, Computer methods in applied mechanics and engineering 194 (39) (2005) 4135–4195.

[2] P. Kagan, A. Fischer, P. Z. Bar-Yoseph, New b-spline finite element approach for geometrical design and mechanical analysis, International Journal for Numerical Methods in Engineering 41 (3) (1998) 435–458.

[3] S. Lipton, J. A. Evans, Y. Bazilevs, T. Elguedj, T. J. Hughes, Robustness of isogeometric structural discretizations under severe mesh distortion, Computer Methods in Applied Mechanics and Engineering 199 (5) (2010) 357–373.

[4] B. Marussig, J. Zechner, G. Beer, T.-P. Fries, Fast isogeometric boundary element method based on independent field approximation, Computer Methods in Applied Mechanics and Engineering 284 (2015) 458–488.

[5] G. Xu, E. Atroshchenko, S. Bordas, Geometry-independent field approximation for spline-based finite element methods, in: Proceedings of the 11th World Congress in Computational Mechanics, 2014.

[6] G. Xu, E. Atroshchenko, W. Ma, S. Bordas, Geometry-independent field approximation: Cad-analysis integration, geometrical exactness and adaptivity, Computer Methods in Applied Mechanics & Engineering.

[7] E. Atroshchenko, G. Xu, S. Tomar, S. Bordas, Weakening the tight coupling between geometry and simulation in isogeometric analysis: from sub-and super-geometric analysis to geometry independent field approximation (gift), arXiv preprint arXiv:1706.06371.

[8] D. Toshniwal, H. Speleers, T. J. Hughes, Smooth cubic spline spaces on unstructured quadrilateral meshes with particular emphasis on extraordinary points: Geometric design and isogeometric analysis considerations, Computer Methods in Applied Mechanics and Engineering.

[9] J. Kiendl, K.-U. Bletzinger, J. Linhard, R. Wüchner, Isogeometric shell analysis with kirchhoff–love elements, Computer Methods in Applied Mechanics and Engineering 198 (49) (2009) 3902–3914.

[10] D. Benson, Y. Bazilevs, M.-C. Hsu, T. Hughes, A large deformation, rotation-free, isogeometric shell, Computer Methods in Applied Mechanics and Engineering 200 (13) (2011) 1367–1378.

[11] D. Benson, Y. Bazilevs, M.-C. Hsu, T. Hughes, Isogeometric shell analysis: the reissner–mindlin shell, Computer Methods in Applied Mechanics and Engineering 199 (5) (2010) 276–289.

[12] D. Benson, S. Hartmann, Y. Bazilevs, M.-C. Hsu, T. Hughes, Blended isogeometric shells, Computer Methods in Applied Mechanics and Engineering 255 (2013) 133–146.

[13] W. Dornisch, S. Klinkel, B. Simeon, Isogeometric reissner–mindlin shell analysis with exactly calculated director vectors, Computer Methods in Applied Mechanics and Engineering 253 (2013) 491–504.

[14] S. Hosseini, J. J. Remmers, C. V. Verhoosel, R. Borst, An isogeometric solid-like shell element for nonlinear analysis, International Journal for Numerical Methods in Engineering 95 (3) (2013) 238–256.

[15] J. A. Cottrell, A. Reali, Y. Bazilevs, T. J. Hughes, Isogeometric analysis of structural vibrations, Computer methods in applied mechanics and engineering 195 (41) (2006) 5257–5296.

[16] J. Kiendl, Y. Bazilevs, M.-C. Hsu, R. Wüchner, K.-U. Bletzinger, The bending strip method for isogeometric analysis of kirchhoff–love shell structures comprised of multiple patches, Computer Methods in Applied Mechanics and Engineering 199 (37) (2010) 2403–2416.

[17] R. Echter, M. Bischoff, Numerical efficiency, locking and unlocking of nurbs finite elements, Computer Methods in Applied Mechanics and Engineering 199 (5) (2010) 374–382.

[18] T. J. Hughes, M. Cohen, M. Haroun, Reduced and selective integration techniques in the finite element analysis of plates, Nuclear Engineering and Design 46 (1) (1978) 203–222.

[19] C. Adam, S. Bouabdallah, M. Zarroug, H. Maitournam, Improved numerical integration for locking treatment in isogeometric structural elements, part I: Beams, Computer Methods in Applied Mechanics and Engineering 279 (2014) 1 – 28.

[20] C. Adam, S. Bouabdallah, M. Zarroug, H. Maitournam, Improved numerical integration for locking treatment in isogeometric structural elements. part II: Plates and shells, Computer Methods in Applied Mechanics and Engineering 284 (2015) 106–137.

[21] C. Adam, S. Bouabdallah, M. Zarroug, H. Maitournam, A reduced integration for reissner-mindlin non-linear shell analysis using t-splines, in: Isogeometric Analysis and Applications 2014, Springer, 2015, pp. 103–125.

[22] T. Elguedj, Y. Bazilevs, V. M. Calo, T. J. R. Hughes, B over-bar and F over-bar projection methods for nearly incompressible linear and non-linear elasticity and plasticity using higher-order nurbs elements, Computer Methods in Applied Mechanics and Engineering 197 (33-40) (2008) 2732–2762.

[23] R. Bouclier, T. Elguedj, A. Combescure, Locking free isogeometric formulations of curved thick beams, Computer Methods in Applied Mechanics and Engineering 245 (2012) 144–162.

[24] R. Bouclier, T. Elguedj, A. Combescure, On the development of nurbs-based isogeometric solid shell elements:

2d problems and preliminary extension to 3d, Computational Mechanics 52 (5) (2013) 1085–1112.

[25] R. Bouclier, T. Elguedj, A. Combescure, Efficient isogeometric nurbs-based solid-shell elements: Mixed formulation and-method, Computer Methods in Applied Mechanics and Engineering 267 (2013) 86–110.

[26] R. Bouclier, T. Elguedj, A. Combescure, An isogeometric locking-free nurbs-based solid-shell element for geometrically nonlinear analysis, International Journal for Numerical Methods in Engineering 101 (10) (2015) 774–808.

[27] T. J. R. Hughes, Generalization of selective integration procedures to anisotropic and nonlinear media, Internat. J. Numer. Methods Engrg. 15 (1980) 1413–1418.

[28] P. Hu, Q. Hu, Y. Xia, Order reduction method for locking free isogeometric analysis of timoshenko beams, Computer Methods in Applied Mechanics and Engineering 308 (2016) 1–22.

[29] R. Echter, B. Oesterle, M. Bischoff, A hierarchic family of isogeometric shell finite elements, Computer Methods in Applied Mechanics and Engineering 254 (2013) 170–180.

[30] K.-U. Bletzinger, M. Bischoff, E. Ramm, A unified approach for shear-locking-free triangular and rectangular shell finite elements, Computers & Structures 75 (3) (2000) 321–334.

[31] F. Brezzi, J. Evans, T. Hughes, L. Marini, New quadrilateral plate elements based on twist-kirchhoff theory, Comput Methods Appl Mech Eng (submitted).

[32] F. Brezzi, L. D. Marini, Virtual element methods for plate bending problems, Computer Methods in Applied Mechanics and Engineering 253 (2013) 455–462.

[33] L. B. da Veiga, C. Lovadina, A. Reali, Avoiding shear locking for the timoshenko beam problem via isogeometric collocation methods, Computer Methods in Applied Mechanics and Engineering 241 (2012) 38–51.

[34] F. Auricchio, L. B. da Veiga, J. Kiendl, C. Lovadina, A. Reali, Locking-free isogeometric collocation methods for spatial timoshenko rods, Computer Methods in Applied Mechanics and Engineering 263 (2013) 113–126.

[35] S. Yin, J. S. Hale, T. Yu, T. Q. Bui, S. P. Bordas, Isogeometric locking-free plate element: a simple first order shear deformation theory for functionally graded plates, Composite Structures 118 (2014) 121–138.

[36] J. Kiendl, F. Auricchio, T. Hughes, A. Reali, Single-variable formulations and isogeometric discretizations for shear deformable beams, Computer Methods in Applied Mechanics and Engineering 284 (2015) 988–1004.

[37] L. Beirão Da Veiga, T. Hughes, J. Kiendl, C. Lovadina, J. Niiranen, A. Reali, H. Speleers, A locking-free model for reissner–mindlin plates: Analysis and isogeometric implementation via nurbs and triangular nurps, Mathematical Models and Methods in Applied Sciences 25 (08) (2015) 1519–1551.

[38] T. J. Mitchell, S. Govindjee, R. L. Taylor, A method for enforcement of Dirichlet boundary conditions in isogeometric analysis, in: Recent Developments and Innovative Applications in Computational Mechanics, Springer, 2011, pp. 283–293.

[39] S. Govindjee, J. Strain, T. J. Mitchell, R. L. Taylor, Convergence of an efficient local least-squares fitting method for bases with compact support, Computer Methods in Applied Mechanics and Engineering 213 (2012) 84–92.

[40] V. P. Nguyen, C. Anitescu, S. P. Bordas, T. Rabczuk, Isogeometric analysis: an overview and computer imple-

mentation aspects, Mathematics and Computers in Simulation 117 (2015) 89–116.

[41] F. Koschnick, M. Bischoff, N. Camprubí, K.-U. Bletzinger, The discrete strain gap method and membrane locking, Computer Methods in Applied Mechanics and Engineering 194 (21) (2005) 2444–2463.

[42] J. Simo, T. Hughes, On the variational foundations of assumed strain methods, Journal of Applied Mechanics 53 (1) (1986) 51–54.

[43] P. Antolin, A. Bressan, A. Buffa, G. Sangalli, An isogeometric method for linear nearly-incompressible elasticity with local stress projection, Computer Methods in Applied Mechanics and Engineering.

[44] B.-Z. Huang, V. B. Shenoy, S. Atluri, A quasi-conforming triangular laminated composite shell element based on a refined first-order theory, Computational mechanics 13 (4) (1994) 295–314.

[45] B. Juettler, U. Langer, A. Mantzaflaris, S. Moore, W. Zulehner, Geometry + simulation modules: Implementing isogeometric analysis, Proc. Appl. Math. Mech. 14 (1) (2014) 961–962.

[46] K. Lee, G. Lim, C. Wang, Thick Lévy plates re-visited, International Journal of Solids and Structures 39 (1) (2002) 127–144.

[47] G. Lim, J. Reddy, On canonical bending relationships for plates, International journal of solids and structures 40 (12) (2003) 3039–3067.

[48] R. H. Macneal, R. L. Harder, A proposed standard set of problems to test finite element accuracy, Finite elements in analysis and design 1 (1) (1985) 3–20.

[49] S. P. Bordas, T. Rabczuk, N.-X. Hung, V. P. Nguyen, S. Natarajan, T. Bog, N. V. Hiep, et al., Strain smoothing in fem and xfem, Computers & structures 88 (23) (2010) 1419–1443.

[50] L. Chen, T. Rabczuk, S. P. A. Bordas, G. Liu, K. Zeng, P. Kerfriden, Extended finite element method with edge-based strain smoothing (esm-xfem) for linear elastic crack growth, Computer Methods in Applied Mechanics and Engineering 209 (2012) 250–265.

[51] M. Surendran, S. Natarajan, S. Bordas, G. Palani, Linear smoothed extended finite element method, arXiv preprint arXiv:1701.03997.